

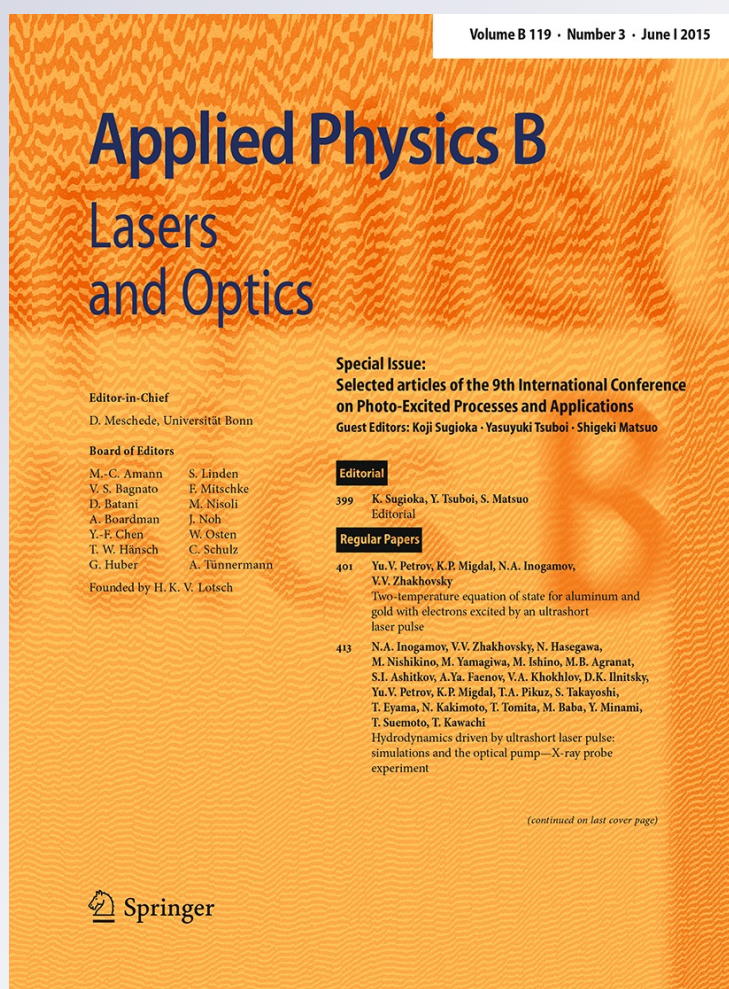
Hydrodynamics driven by ultrashort laser pulse: simulations and the optical pump—X-ray probe experiment

**N. A. Inogamov, V. V. Zhakhovsky,
N. Hasegawa, M. Nishikino,
M. Yamagiwa, M. Ishino, M. B. Agranat,
S. I. Ashitkov, A. Ya. Faenov, et al.**

Applied Physics B
Lasers and Optics

ISSN 0946-2171
Volume 119
Number 3

Appl. Phys. B (2015) 119:413–419
DOI 10.1007/s00340-015-6039-7



Your article is protected by copyright and all rights are held exclusively by Springer-Verlag Berlin Heidelberg. This e-offprint is for personal use only and shall not be self-archived in electronic repositories. If you wish to self-archive your article, please use the accepted manuscript version for posting on your own website. You may further deposit the accepted manuscript version in any repository, provided it is only made publicly available 12 months after official publication or later and provided acknowledgement is given to the original source of publication and a link is inserted to the published article on Springer's website. The link must be accompanied by the following text: "The final publication is available at link.springer.com".

Hydrodynamics driven by ultrashort laser pulse: simulations and the optical pump—X-ray probe experiment

N. A. Inogamov · V. V. Zhakhovsky · N. Hasegawa · M. Nishikino · M. Yamagiwa · M. Ishino · M. B. Agranat · S. I. Ashitkov · A. Ya. Faenov · V. A. Khokhlov · D. K. Ilitsky · Yu. V. Petrov · K. P. Migdal · T. A. Pikuz · S. Takayoshi · T. Eyama · N. Kakimoto · T. Tomita · M. Baba · Y. Minami · T. Suemoto · T. Kawachi

Received: 10 October 2014 / Accepted: 3 February 2015 / Published online: 17 February 2015
© Springer-Verlag Berlin Heidelberg 2015

Abstract Spatial structures of ablative mass flow produced by femtosecond laser pulses are studied. In experiments with a gold film, the Ti:sapp laser pulse having a focal size of 100 microns on a target was used, while a soft X-ray probe pulse was utilized for diagnostics. The experimental data are compared with simulated mass flows obtained by two-temperature hydrodynamics and molecular dynamics methods. Simulation shows evolution of a thin surface layer pressurized after electron–ion thermalization, which leads to melting, cavitation and formation of spallation liquid layer. The calculated asymptotic surface velocity of this layer as a function of fluence is in reasonably good agreement with experimental data.

1 Introduction

Lasers with ultrashort pulses have a wide range of well-acknowledged important applications from nanoscience

to material modifications and medicine [1]. To develop these applications, the physics of ultrashort pulse–matter interaction should be studied. The first signal of what is going on under the fast illumination comes thanks to the paper [2], where the number of Newton rings grows with time during observation. After the paper [3], it was understood that these rings manifest existence and development of a cavity under an illuminated spot—the illuminated spot releases off a thin surface layer forming a spallation shell flying away; see [3–13]. Newton interference takes place between the shell and the remnant of the target. The shell flies away, distance between the dome-like shell and target increases resulting in increase of the number of Newton rings with time. The shell is very thin (of the order of skin-depth ~10–20 nm) layer allowing light passes it twice at least. Therefore, we can term this phenomenon as nanospallation. Experiments described below are based on a unique pump–probe technique with an X-ray probe.

N. A. Inogamov (✉) · V. A. Khokhlov · Y. V. Petrov
L. D. Landau Institute for Theoretical Physics, Russian Academy of Sciences, Chernogolovka, Russia
e-mail: nailinogamov@gmail.com

N. A. Inogamov · V. V. Zhakhovsky · D. K. Ilitsky · K. P. Migdal
All-Russia Research Institute of Automatics, ROSATOM,
Moscow, Russia

V. V. Zhakhovsky · M. B. Agranat · S. I. Ashitkov · A. Y. Faenov · T. A. Pikuz
Joint Institute for High Temperatures, Russian Academy of Sciences, Moscow, Russia

N. Hasegawa · M. Nishikino · M. Yamagiwa · M. Ishino · T. Kawachi
Quantum Beam Science Directorate, Japan Atomic Energy Agency, Kizugawa, Kyoto, Japan

A. Y. Faenov
Institute for Academic Initiatives, Osaka University, Suita, Osaka, Japan

T. A. Pikuz
Graduate School of Engineering, Osaka University, Suita, Osaka, Japan

S. Takayoshi · T. Eyama · N. Kakimoto · T. Tomita
Faculty of Engineering, The University of Tokushima,
Tokushima, Japan

M. Baba · Y. Minami · T. Suemoto
Institute of Solid State Physics, University of Tokyo, Kashiwa, Chiba, Japan

Table 1 Parameters of MD simulations

Run	L_y (nm)	L_z (nm)	$N_{\text{at}} \times 10^6$	F_{abs} (mJ/cm ²)	t_{max} (ps)	v_{surf}^{∞} (m/s)	$d_{\text{spall}}^{\infty}$ (nm)	$T_{\text{spall}}^{\infty}$ (kK)
1	11.8	12.1	8.4	118.1	165	0	–	–
2	11.8	12.1	8.4	137.4	571	128.5	92	1.48
3	120	16.2	115	136.9	1765	130	80.3	1.7
4	120	16.2	115	192.6	636	315	35	2.61
5	120	16.2	115	201.5	688	321	39	2.68
6	120	16.2	115	295.4	819	540	32	3.47

Thickness of film was $L_x = 1000$ nm in all runs. Here v_{surf}^{∞} is a center of mass velocity of a spallation plate (final velocity); $T_{\text{spall}}^{\infty}$ is a “final” average temperature inside the spallation plate at a time interval up to ~ 10 – 3 s when radiation losses $\sigma_{\text{SB}} T_{\text{spall}}^4$ becomes significant, σ_{SB} is the Stefan–Boltzmann constant; $d_{\text{spall}}^{\infty}$ is a final average thickness of the spallation plate (the plate undergo weak slowly decaying acoustic oscillations, see Fig. 5)

The pump–probe technique with an X-ray probe [14–17] is a new approach relative to the pump–probe technique used in [2]. The probe pulse is changed from optical to a soft X-ray ($h\nu = 89$ eV, $\lambda = 13.9$ nm) pulse. This method is much more complicated than used in [2], but it has important advantages. The advantages of new approach are as follows: First, using of a X-ray probe allows to begin observation of the Newton rings much earlier because the wavelength of X-ray probe is one-two orders of magnitude smaller than optical wavelengths. Second, thanks to refractive shadowgraph, the expansion of plume is followed up by X-probe to much larger spatiotemporal scales. In [2], the largest observation times were ~ 1 – 10 ns, while the new technique continues tracking of flow up to the times of the order of microsecond. Late time the X-shadowgraph is feasible because X-ray absorption is proportional to the mass along a ray path, while optical absorption decreases as material fragments into small droplets. Nevertheless, the shadowgraph can be obtained also by the optical probe in principle, but this was not done up to now.

In [2], an ultrashort laser pulse is divided into two pulses. One serves as a pump, while the other passes another optical path from laser to target and serves as a probe. This splitting simplifies a problem of exact synchronization of two pulses. In our case, two optical and one soft X-ray lasers are employed [14–17]. Synchronization of them is non-trivial problem. Optical Nd-laser creates two coaxial plasma columns, they irradiate out a soft X-ray pulse along a common axis of columns [14–17]. The X-pulse has small angular divergence (few mrad), small frequency spreading ($\Delta\lambda/\lambda < 10^{-4}$), and high coherence properties [14–17]. Ti:sapp system is external relative to the system from Nd-laser and plasma columns. These two systems are synchronized to form a generating and measurement device (pump–probe device). Another solved [14–17] non-trivial problem is connected with focusing and construction of the X-ray image of an illuminated spot.

There is qualitative understanding of ablation flow with dome-like shell (or cupola) and two-phase mixture inside [3–13]. Quantitative description is necessary to describe results of the X-probe experiment. In this short paper, we present large-scale molecular dynamics (MD) simulations of ablation flow starting from temperature profiles calculated by hydrodynamics simulations using the full-scale two-temperature physics, see details of methods in [18–21].

2 Formulation of the problem

Let us consider action of a near infrared (Ti:sapp) ultrashort laser pulse (duration $\tau_L = 70$ fs) on a gold film. The detailed two-temperature physics of gold is presented in [21]. Two-temperature hydrodynamics (2T-HD) is used to model the earliest two-temperature stage of material in order to obtain an initial profile of temperature to continue long-time evolution in MD simulation, in the same way as see [18–21]. The interatomic EAM potential for gold [22] used in our MD simulations is identical to that used in [19]. Parameters of MD simulations are summarized in Table 1. Results of simulations are shown in Figs. 1, 2, 3, 4, 5, 6, 7 and 8. In Fig. 1, two maps of central symmetry parameter, depending on the local order in atom coordination environment, are presented.

Fluence distribution along a target surface is assumed to be homogeneous, and hydrodynamic motion proceeds along the direction x only. Periodic boundary conditions in y and z directions are imposed in MD cell. In Fig. 1, two maps in the $x \times y$ -plane are shown. Direction z is perpendicular to the plane of figure. The spatial scale L_z along direction z is enough large, see Table 1. It is ≈ 40 atomic monolayers in runs 3–6. Therefore, nucleation of voids (small bubbles) begins and evolves in 3D conditions close to real situation in the stretched molten



Fig. 1 Maps of central symmetry parameter showing local order in ion subsystem in MD simulation with the absorbed fluence $F_{\text{abs}} = 136.9 \text{ mJ/cm}^2$, see run 3 in Table 1. Red colors correspond to molten gold, green to solid. $F_{\text{abs}}/F_{\text{abs|abl}} = 1.16$, $v_{\text{surf}}^\infty = 130 \text{ m/s}$, $T_{\text{spall}}^\infty = 1.7 \text{ kK}$, $d_{\text{spall}} = 80.3 \text{ nm}$. Here $F_{\text{abs|abl}}$ is a thermomechanical ablation threshold, which is equal to 118 mJ/cm^2 according our simulations

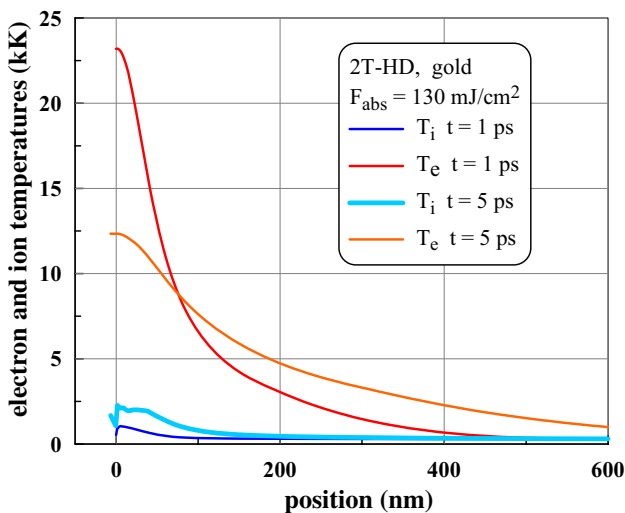


Fig. 2 Cooling of electrons as a result of energy transfer to ions and heat conduction to the bulk

gold. The 3D evolution of flow with a two-phase mixture continues up to a stage when the bubble's diameters grow to the size $L_z \sim 10 \text{ nm}$ of MD cell. After that the periodical boundary condition along z -axis begins to affect on evolution of the foam resulting in gradual transition from 3D to 2D-type evolution. Resistance to stretching of the 2D foam is weaker than the 3D foam. But as it will be shown below (comparisons of small and large scales runs 2 and 3) the bubbles are already large enough and surface tension effects are rather weak at this stage.

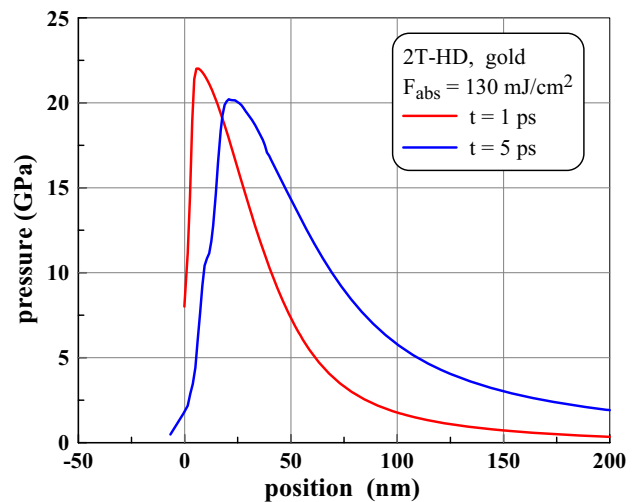


Fig. 3 Evolution of pressure at a two-temperature stage

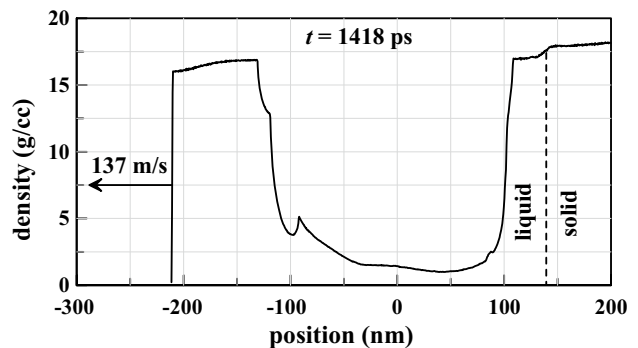


Fig. 4 Instant density profile when spallation plate flying ahead almost separates from a target, $F_{\text{abs}} = 136.9 \text{ mJ/cm}^2$. This instant corresponds to the bottom map in Fig. 1. After separation, the momentum and velocity of the center of mass stop their decreasing with time. For large spot, we neglect the capillary deceleration connected with the surface tension acting along a shell of a dome. The arrow shows the instant velocity of the external surface $v_{\text{surf}}(t)$ of spallation plate

3 Simulation results

Prior to a pump pulse, the equilibrium crystalline *fcc* gold of normal density is prepared in simulation cell. Very short lasting pump transfers energy F_{abs} to electron subsystem and is switched off. This transfer initiates two processes [18, 21, 23]. There is a process of electron-ion relaxation: heating of ions through cooling of electrons, see Fig. 2. As a result the local electron T_e and ion T_i temperatures converge until the end of two-temperature stage at $T_e \approx T_i$. The second process corresponds to an electron

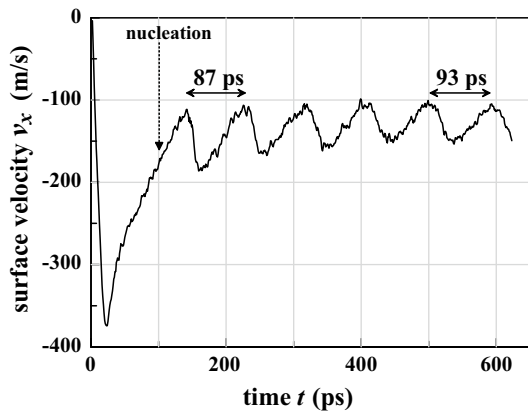


Fig. 5 Temporal behavior of the external surface velocity $v_{\text{surf}}(t)$; $F_{\text{abs}} = 136.9 \text{ mJ/cm}^2$. This velocity is defined in Fig. 4. Velocity $v_{\text{surf}}(t)$ sharply increases during two-temperature stage and achieves its maximum (here we speak about absolute value $|v_{\text{surf}}(t)|$). After that resistance of condensed matter to stretching decreases velocity $v_{\text{surf}}(t)$. At the instant marked by the arrow “nucleation” a nucleation starts in stretched and molten gold [19]. A weak shock named spallation pulse arrives at the external surface in the instant when the first minimum of expansion velocity $|v_{\text{surf}}(t)|$ is achieved. This shock is sent from a nucleation layer

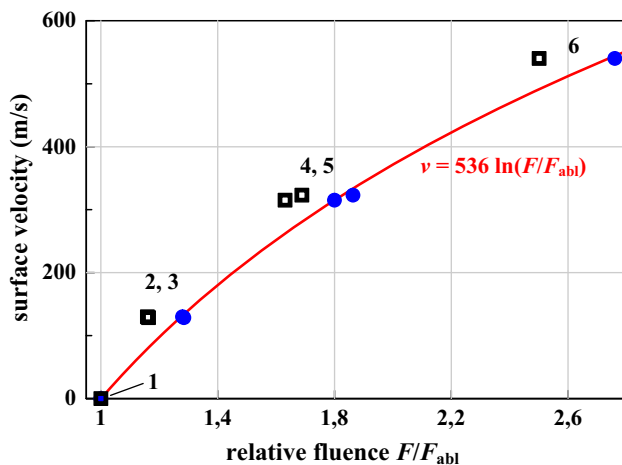


Fig. 6 Comparison of simulations (empty squares) and experiments (generalized as a continuous curve). The curve is defined by expression $v = 536 \ln(F_{\text{inc}}/F_{\text{inc|abl}})$ [m/s]. Final velocities $|v_{\text{surf}}^{\infty}|$ of spallation plates are presented. The plates achieve these velocities after separation from remnants of irradiated target. Circles correspond to normalization $F_{\text{abs}}/F_{\text{abs|abl}}$ for another threshold $F_{\text{abs|abl}} = 107 \text{ mJ/cm}^2$. This value is different from the ablation threshold $F_{\text{abs|abl}} = 118 \text{ mJ/cm}^2$ taken for empty squares, see text for explanations. Numbers enumerate MD runs presented in Table 1

heat wave penetrating into the bulk target, which creates a heated layer with thickness d_T . Evolution of pressure profile during the two-temperature stage is shown in Fig. 3.

An absorbed fluence F_{abs} is used as a main parameter in our 2T-HD and molecular dynamics (MD) simulations.

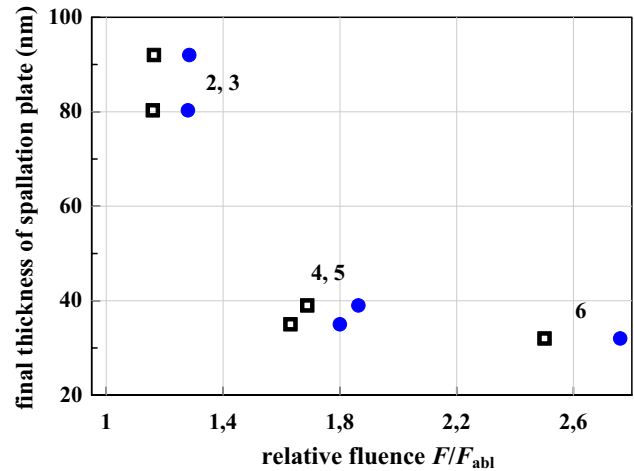


Fig. 7 Asymptotic values of thicknesses d_{spall} of the spallation plates as function of normalized fluence $F_{\text{abs}}/F_{\text{abs|abl}}$. Empty squares correspond to normalization to the ablation threshold $F_{\text{abs|abl}} = 118 \text{ mJ/cm}^2$, for circles the normalization is $F_{\text{abs|abl}} = 107 \text{ mJ/cm}^2$. Numbers enumerate MD runs presented in Table 1

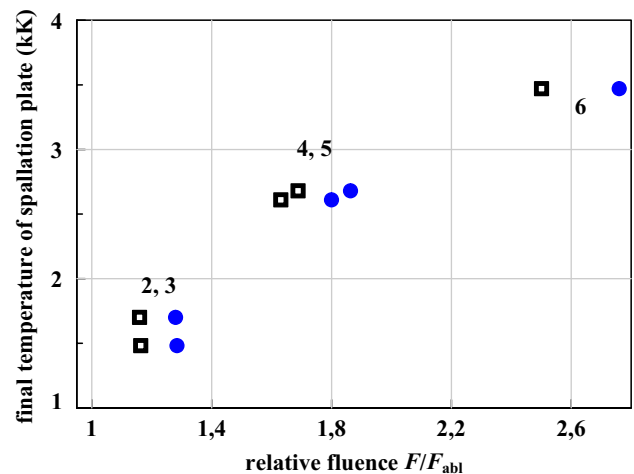


Fig. 8 Final temperatures T_{spall} of the spallation plate as a function of normalized fluence $F_{\text{abs}}/F_{\text{abs|abl}}$. Empty squares correspond to normalization to the ablation threshold $F_{\text{abs|abl}} = 118 \text{ mJ/cm}^2$, for circles the normalization is $F_{\text{abs|abl}} = 107 \text{ mJ/cm}^2$. Numbers enumerate MD runs presented in Table 1

Question about relation between absorbed and incident pump fluences is not easy because in our range of rather high intensities a linear dependence $F_{\text{abs}} = AF_{\text{inc}}$ may not be satisfied [24], here A is an absorptance. Linear dependence is satisfied for low laser intensities [24]. In the linear case, the absorptance is defined by the Fresnel formulas. In 2T-HD simulations, a skin thickness of 15 nm has been taken as a penetration depth of photons. A gold target was at the room temperature of 293 K before a pump pulse arrival to a surface.

Hydrodynamic motion at the two-temperature stage smoothly transits to “common” one-temperature hydrodynamic motion. Heat conductivity enhanced during the two-temperature stage returns to its one-temperature value. This value is rather small, therefore fast propagation of heat wave during the first few picoseconds is changed to very slow (subsonic) propagation lasting nanoseconds up to full cooling of surface layer down to room temperatures as a result of heat transfer into the bulk of a thick film, in which the film thickness is much larger than the heated layer d_T . Pressurized surface layer created during the fast (supersonic) heating releases in the direction toward vacuum as well as in opposite direction toward the bulk [19].

The release into the vacuum side accelerates the external surface as it is shown in Figs. 4 and 5. Expansion into the vacuum decreases local density of gold inside the heated layer below its equilibrium density at the zero pressure. The equilibrium density is defined by the local temperature (expansion along an adiabatic curve). Expansion below the equilibrium density causes formation of negative pressure field. This field acts to decelerate expansion. Therefore, the velocity $|v_{\text{surf}}(t)|$ in Fig. 5 begins to decrease after the first maximum.

Figure 5 presents a simulation with fluence above the ablation threshold, at which the kinetic energy collected during acceleration overcomes the work done by the negative pressure against expansion of gold. This work continues up to the instant of nucleation of voids. During short (few picosecond) nucleation stage, the pressure in the nucleation layer drops to zero and accumulation of work against expansion stops. But time t_{sp} is necessary to spallation pulse (weak shock propagating from nucleation layer) to pass distance d_{sp} between the nucleation layer and external surface (the left boundary of density profile in Fig. 4). During this propagation time, the deceleration of surface continues—velocity $|v_{\text{surf}}(t)|$ continues to decrease after the instant “nucleation” shown in Fig. 5. Thus the velocity $|v_{\text{surf}}(t)|$ drops below the velocity of the center of mass of a spallation plate. This causes acoustic oscillations, shown in Fig. 5, inside the spallation plate. The period of these oscillations is $\approx 2 t_{\text{sp}}$ because the period is defined by a period which is necessary for the double pass of thickness of spallation plate d_{sp} .

The velocity of surface of a spallation plate $v_{\text{surf}}(t)$ and the velocity of the center of mass of the plate v_{cm} both are shown in Fig. 5. The latter is calculated from total momentum and total mass of the spallation plate. Due to acoustic oscillations the velocities v_{surf} and v_{cm} differ. Compare v_{surf} in Fig. 4 and in Table 1 (run 3, $F_{\text{abs}} = 136.9 \text{ mJ/cm}^2$). Total amplitude of the velocity oscillations $\approx 70 \text{ m/s}$ in Fig. 5 is significant.

Velocities v_{surf} and v_{cm} become equal when the oscillations totally decay later and the spallation plate takes off all material ties with a target. Those ties shown in Fig. 1 are liquid membranes which put together the spallation plate

and the target. Let us mention that the oscillations of the spallation plate for a thicker plate (\sim millimeter) [25–27] decay much faster at the same velocities, see examples of a rear-side spallation from a solid state matter in [25–27]. In Fig. 5, the oscillation amplitude decreases approximately by 30 % after five oscillations. If we approximate the decay by a geometric progression (an exponential trend) $1, q, q^2, \dots$ with a step q then in our simulations $q \approx 1.05$. In the mm-cases [25–27], this value is higher $q \sim 1.5$ – 3 . Therefore, the decay to 1 % of initial amplitude takes place after $4.6/(q - 1) \approx 10^2$ oscillations in our simulations ($\sim 10 \text{ ns}$), while in the mm-cases, the ~ 1 – 10 oscillations are required.

Simulation shown in Fig. 1 is one of the longest in time. But even for 1.5 ns after a pump pulse the ties between the spallation plate and the bulk target survive. The imprints of bubbles adjoining to the spallation plate are clearly seen in a density profile in Fig. 4 if we compare the bottom panel of Figs. 1 and 4. The first sharp decrease of density in Fig. 4 is an image of a left tip of a small bubble inside jet—a membrane connecting the spallation plate and the target in the bottom panel in Fig. 1. Length of membrane is more than 200 nm at the time of 1.5 ns, see Fig. 4. The second drop down in Fig. 4 represents the tip of the large bubble adjoining to the spallation plate. A small maximum near the point $x \approx -90 \text{ nm}$ in Fig. 4 is the right tip of the small bubble.

Long lasting and spatially large-scale MD simulations are necessary to achieve an asymptotic state of flight of a spallation plate. Final values of mass, momentum, and internal energy (we neglect radiative losses) establish after mechanical and thermal separation from target (breaking of membranes) and dissipation of kinetic energy of oscillations (this is small addition to internal energy). Only one run listed in Table 1 transfers into the state with broken membranes and the free spallation plate. This is the run 2 with the smallest lateral scales. It is much more easy to break membrane in the case of small lateral dimensions L_y, L_z of MD computational cell, than in the case of simulation with large spatial scales. Runs with large spatial scales help to estimate a role of surface tension of membranes in the deceleration of a spallation plate. We see that the small run 2 and large run 3 in Table 1 differ slightly. This means that estimates of asymptotic values for $v_{\text{spall}}, d_{\text{spall}}$, and T_{spall} are valid. At a later stage the dynamic influence of membranes is very weak and we can neglect the fact that they are still unbroken.

4 Comparison of simulations and experiments

Comparison of results of combined hydrodynamic and molecular dynamics simulations with X-probe experiments

is shown in Fig. 6. The curve $v = 536 \ln(F_{\text{inc}}/F_{\text{inc}|_{\text{abl}}})$ m/s presents experimental data with approximately $\pm 5\%$ error. This curve sum up all experimental data obtained thanks to Newton rings, X-ray interferometry, and X-ray shadow-graph measurements. Figure 6 illustrates dependence of final velocity $|v_{\text{surf}}^{\infty}|$ on energy of a pump pulse.

Final velocities $|v_{\text{surf}}^{\infty}|$ in Fig. 6 taken from the X-probe experiment are given as a function of incident fluence F_{inc} normalized to the threshold value $F_{\text{inc}|_{\text{abl}}}$ of incident fluence, where the note $|_{\text{abl}}$ means that this value corresponds to the ablation threshold. Distribution of incident fluence F_{inc} along an illuminated spot was carefully measured in experiments [14–17]. An absorption coefficients $A(F_{\text{abs}}) = 1 - R = F_{\text{abs}}/F_{\text{inc}}$ for Ti:sapp laser will be measured in near future. It is the significant function of fluence F_{inc} in our range of fluences. Coefficient A in our range of fluences is few times larger than the value obtained from Fresnel formula [28]. This was shown in paper [28] for the case of Cr:forsterite laser. Fresnel formula gives $A(F_{\text{abs}} \rightarrow 0, h\nu = 1 \text{ eV}) = 2\%$ for Cr:forsterite and $A(F_{\text{abs}} \rightarrow 0, h\nu = 1.5 \text{ eV}) = 2.5\%$ for Ti:sapp. While $A(F_{\text{abs}} \sim 1 \text{ J/cm}^2, h\nu = 1 \text{ eV}) \approx 10\%$ [23, 28]—we see that absorption is five times higher!

Simulation results shown in Fig. 6 by squares are plotted as a function of absorbed fluence F_{abs} normalized to the ablation threshold $F_{\text{abs}|_{\text{abl}}}$ for absorbed fluence. We can plot simulation and experimental velocities together on Fig. 6, assuming the absorption coefficient is a constant in the range of considered fluences. Then $F_{\text{abs}}/F_{\text{abs}|_{\text{abl}}} = F_{\text{inc}}/F_{\text{inc}|_{\text{abl}}}$.

According to MD simulations, the ablation threshold for absorbed fluence F_{abs} is located between the first left square in Fig. 6 and the second one. The first square corresponds to $F_{\text{abs}} = 118 \text{ mJ/cm}^2$. Final velocity $|v_{\text{surf}}^{\infty}|$ for this value of absorbed fluence equals to zero. The second square corresponds to $F_{\text{abs}} = 137.4 \text{ mJ/cm}^2$ and $|v_{\text{surf}}^{\infty}| = 128.5 \text{ m/s}$. Other parameters are listed in Table 1, this is the run 2. If we take the value of 118 mJ/cm^2 as an ablation threshold on absorbed fluence $F_{\text{abs}|_{\text{abl}}}$ for the second square, then the ratio $F_{\text{abs}}/F_{\text{abs}|_{\text{abl}}}$ is equal to 1.163 for the second square as it is plotted in Fig. 6. Of course, the ablation threshold of 118 mJ/cm^2 is the least possible value for the ablation threshold $F_{\text{abs}|_{\text{abl}}}$. In [19, 23, 28] the ablation threshold $F_{\text{abs}|_{\text{abl}}}$ for gold was supposed to be $\approx 130 \text{ mJ/cm}^2$. Let us mention in this connection that the definition of the threshold $F_{\text{abs}|_{\text{abl}}}$ with 10% accuracy is a difficult problem. Experimentalists define the threshold $F_{\text{inc}|_{\text{abl}}}$ using an incidence fluence. It is not easy problem to measure the absorption coefficient at the elevated light fluxes with high enough accuracy, and the small inaccuracies affect evaluation of the absorbed fluence.

The range of near threshold fluences from 118 to $\approx 130 \text{ mJ/cm}^2$ has to be studied additionally. Because

small variation of threshold $F_{\text{abs}|_{\text{abl}}}$ significantly influences results. In Fig. 6, circles present the same simulation results as shown by squares but now normalized to another slightly different threshold value: 107 mJ/cm^2 (circles) versus the ablation threshold of 118 mJ/cm^2 for squares. It is significant to emphasize that the near threshold region is not very narrow, it covers a few percent range. The nucleation threshold (when the first nuclei are formed inside stretched molten gold) is few percent below an ablation threshold $F_{\text{abs}|_{\text{abl}}}$, see papers [12, 29, 30] about splitting of nucleation and ablation thresholds. This splitting signals that resistance of foam to stretching introduces appreciable contribution to deceleration of spallation plate.

Experimental value for ablation threshold on incident fluence is $F_{\text{inc}|_{\text{abl}}} = 880 \text{ mJ/cm}^2$ for X-probe experiments. As was said above, a Ti:sapp laser $\lambda = 800 \text{ nm}$ was used as a pump. If we take the threshold $F_{\text{abs}|_{\text{abl}}} = 118 \text{ mJ/cm}^2$ then the absorption coefficient $A(\lambda = 800, F_{\text{inc}} = 880) = 118/880$ is 13%. This seems reasonable, because for the first harmonics of the Cr:forsterite laser we have $A(\lambda = 1240, F_{\text{inc}} = 1300) = 10\%$ [23, 28], while the Fresnel absorptions are $A_{\text{Fres}}(\lambda = 800) = 2.5\%$ and $A_{\text{Fres}}(\lambda = 1240) = 2\%$ —that is the Ti:sapp Fresnel absorption is 5/4 higher then in case of Cr:forsterite. Perhaps the stronger absorption at higher fluences keeps this Fresnel ratio.

Figures 6, 7 and 8 present the results concerning asymptotic velocity v_{spall} , thickness of spallation plate d_{spall} , and temperature of spallation plate T_{spall} before a radiative cooling, see also Table 1. Qualitative behavior of function $d_{\text{spall}}(F_{\text{abs}})$ is known [11, 12, 23]. There are two thresholds. First is the ablation threshold $F_{\text{abs}|_{\text{abl}}}$, at which a spallation plate $d_{\text{spall}|_{\text{abl}}}$ is formed. Increasing the absorbed fluence F_{abs} in the interval $F_{\text{abs}|_{\text{abl}}} < F_{\text{abs}} < F_{\text{abs}|_{\text{ev}}}$ decreases monotonically the thickness $d_{\text{spall}}(F_{\text{abs}})$. Finally, in the point $F_{\text{abs}|_{\text{ev}}}$ the spallation plate disappears: $d_{\text{spall}}(F_{\text{abs}|_{\text{ev}}}) = 0$. Another threshold $F_{\text{abs}|_{\text{ev}}}$ is called as “evaporation” (ev) threshold in [23] because the spallation plate disappears. It is interesting that according to our data (see Figs. 6, 7) the spallation plate survives even at the triple excess above the ablation threshold in gold.

5 Discussion and conclusion

The main goal of this paper is to check accuracy of combined 2T-HD and molecular dynamics (MD) simulations (2T-HD/MD approach) by comparing the 2T-HD/MD results with experimental data obtained by recently developed powerful tool based on X-probe diagnostics [14–17]. Sections 2–4 above present simulations and experiments and their comparison, see Fig. 6. Simulation and X-probe

experiment both have their own shortcomings. Therefore, the careful comparison is very valuable because it gives us improved and more quantitative conceptions of the laser-matter interaction. Comparisons also inform us what we can do to increase abilities of simulations and experiments. From discussions in Sects. 2–4, it follows that measuring of absorption coefficient as function of incident fluence for working wavelength of a pump laser is necessary for accurate quantitative comparison with simulations. Another problem that should be solved concerns region of fluences near ablation threshold.

Summing up the work done, we have to say that there is an encouraging agreement between the theoretical model and experiments. This means that we have taken the first step in the right direction.

Acknowledgments The research (NAI, VVZh, VAKh, DKI, YVP, KPM, AYF, TAP) has been performed under financial support from Russian Science Foundation (RSCF) (Project No. 14-19-01599). This work (except NAI, VVZh, VAKh, DKI, YVP, KPM) was partly supported by Grant-in-Aid for Scientific Research (B), No. 25289244 (2013), from MEXT and bilateral program: Japan Society for the Promotion of Science (JSPA) and Russian Academy of Sciences (RAS) under the JSPS-RAS Joint Research Program (RFBR Grant 14-02-92107).

References

- 9th International Conference on Photo-Excited Processes and Applications, Program & Technical Digest, September 29–October 3, (2014), Matsue Japan. Conference Chairs: Koji Sugioka, Yasuyuki Tsuboi. icpepa9.com
- K. Sokolowski-Tinten, J. Bialkowski, A. Cavalleri et al., *Phys. Rev. Lett.* **81**(1), 224–227 (1998)
- N.A. Inogamov, Y.V. Petrov, S.I. Anisimov et al., *JETP Lett.* **69**(4), 310–316 (1999)
- S.I. Anisimov, N.A. Inogamov, A.M. Oparin et al., *Appl. Phys. A* **69**, 617–620 (1999)
- V.V. Zhakhovskii, K. Nishihara, S.I. Anisimov, N.A. Inogamov, *JETP Lett.* **71**(4), 167–172 (2000)
- D.S. Ivanov, L.V. Zhigilei, *Phys. Rev. B* **68**, 064114 (2003)
- S.I. Anisimov, V.V. Zhakhovskii, N.A. Inogamov et al., *JETP Lett.* **77**(11), 606–610 (2003)
- P. Lorazo, L.J. Lewis, M. Meunier, *Phys. Rev. Lett.* **91**(22), 225502 (2003). (4 pages)
- M. Gill-Comeau, L.J. Lewis, *Phys. Rev. B* **84**, 224110 (2011)
- N.N. Nedialkov, P.A. Atanasov, S. Amoruso, R. Bruzzese, X. Wang, *Appl. Surf. Sci.* **253**, 7761–7766 (2007)
- L.V. Zhigilei, Z. Lin, D.S. Ivanov, *J. Phys. Chem. C* **113**, 11892–11906 (2009)
- C. Wu, L.V. Zhigilei, *Appl. Phys. A* **114**, 11–32 (2014)
- M.E. Povarnitsyn, T.E. Itina, M. Sentis, K.V. Khishchenko, P.R. Levashov, *Phys. Rev. B* **75**, 235414 (2007)
- T. Suemoto, K. Terakawa, Y. Ochi et al., *Opt. Express* **18**(13), 14114–14122 (2010)
- T. Tomita, M. Yamamoto, N. Hasegawa et al., *Opt. Express* **20**(28), 29329–29337 (2012)
- M. Baba, M. Nishikino, N. Hasegawa et al., *Jpn. J. Appl. Phys.* **53**, 080302 (2014). (4 pages)
- T. Tomita, M. Nishikino, N. Hasegawa et al., *J. Laser Micro Nanoeng.* **9**(2), 137–142 (2014)
- N.A. Inogamov, Y.V. Petrov, V.V. Zhakhovskiy et al., in *International Symposium High Power Laser Ablation 2012. AIP Conference Proceedings* vol 1464, (2012), pp. 593–608. doi:[10.1063/1.4739912](https://doi.org/10.1063/1.4739912)
- B.J. Demaske, V.V. Zhakhovskiy, N.A. Inogamov, I.I. Oleynik, *Phys. Rev. B* **82**, 064113 (2010)
- B.J. Demaske, V.V. Zhakhovskiy, N.A. Inogamov, I.I. Oleynik, *Phys. Rev. B* **87**, 054109 (2013)
- N.A. Inogamov, V.V. Zhakhovskiy, V.A. Khokhlov, *Zhurnal Exp. Theor. Fiziki* **147**(1), 20–56 (2015). (In Russian, will be translated into English soon)
- N.A. Inogamov, V.V. Zhakhovskii, S.I. Ashitkov et al., *JETP* **107**(1), 1–19 (2008)
- W.-L. Chan, R.S. Averback, D.G. Cahill, *Appl. Phys. A* **97**, 287–294 (2009)
- V.V. Zhakhovskii, N.A. Inogamov, Y.V. Petrov, S.I. Ashitkov, K. Nishihara, *Appl. Surf. Sci.* **255**(24), 9592–9596 (2009)
- T. Antoun, L. Seaman, D.R. Curran, G.I. Kanel, S.V. Razorenov, A.V. Utkin, *Spall Fracture* (Springer, New York, 2003)
- G.I. Kanel, S.V. Razorenov, V.E. Fortov, *Shock Wave Phenomena and the Properties of Condensed Matter* (Springer, New York, 2004)
- G.I. Kanel, V.E. Fortov, S.V. Razorenov, *Phys. Uspekhi* **50**, 771–791 (2007)
- N.A. Inogamov, V.V. Zhakhovskii, S.I. Ashitkov et al., *Appl. Surf. Sci.* **255**(24), 9712–9716 (2009). [arXiv:0812.2965](https://arxiv.org/abs/0812.2965) (physics. optics)
- V.V. Zhakhovskii, N.A. Inogamov, K. Nishihara, *JETP Lett.* **87**(8), 423–427 (2008)
- S.I. Ashitkov, N.A. Inogamov, V.V. Zhakhovskiy et al., *JETP Lett.* **95**(4), 176–181 (2012)